

ElecTra Code: Full-Band Electronic Transport Properties of Materials

Patrizio Graziosi¹⁻², Zhen Li², and Neophytos Neophytou²

¹ CNR – ISMN, Bologna, Italy

² School of Engineering, University of Warwick, UK

Abstract

This paper introduces *ElecTra*, an open-source code which solves the linearized Boltzmann transport equation in the relaxation time approximation for charge carriers in a full-band electronic structure of arbitrary complexity, including their energy, momentum, and band-index dependence. *ElecTra* stands for ‘ELECTronic TRANsport’ and computes the electronic and thermoelectric transport coefficients electrical conductivity, Seebeck coefficient, electronic thermal conductivity, and mobility, for semiconductor materials, for both unipolar and bipolar (small bandgap) materials. The code uses computed full-bands and relevant scattering parameters as inputs and considers single crystal materials in 3D and 2D. The present version of the code (v1) considers: i) elastic scattering with acoustic phonons and inelastic scattering with non-polar optical phonons in the deformation potential approximation, ii) inelastic scattering with polar phonons, iii) scattering with ionized dopants, and iv) alloy scattering. The user is given the option of intra- and inter-valley scattering considerations. The simulation output also includes relevant relaxation times and mean-free-paths. The transport quantities are computed as a function of Fermi level position, doping density, and temperature. *ElecTra* can interface with any DFT code which saves the electronic structure in the ‘.bxsf’ format. In this paper *ElecTra* is validated against ideal electronic transport situations of known analytical solutions, existing codes employing the constant relaxation time approximation, as well as experimentally well-assessed materials such as Si, Ge, SiGe, and GaAs.

Program summary

Program title: *ElecTra* – Electronic Transport simulation lab

Program Files doi:

CPC Library link to program files:

Developer’s repository link:

Licensing provisions: GPLv3

Programming Language: MATLAB®

Nature of the problem: computing the electronic and thermoelectric charge transport coefficients of materials with arbitrary complex full-band electronic structures, considering the carrier energy-, momentum-, and band-dependence of the scattering rates.

Solution method: Semiclassical Linearized Boltzmann transport equation, with electronic structures (DFT or analytical) as input, formed into constant-energy surfaces, with scattering rates evaluated using Fermi's Golden Rule.

Programming interface: any DFT code which saves data in the '.bxsf' format.

RAM: a case study for a half-Heusler bandstructure on a $51 \times 51 \times 51$ k -mesh, 2Gb per processor is needed

Running time: for the example above, depending on the number and complexity of the scattering mechanisms and the number of simulated Fermi levels and temperatures considered, the time needed varies from ~ 1 hour on a desktop PC or laptop (light simulations), to 5-10 hours on an HPC with 30-45 cores (heavy simulations). Using the constant relaxation time and constant mean-free-path approximations on a desktop PC or laptop, the running time is of the order of minutes.

1. Introduction

Electronic and thermoelectric transport simulations in novel complex bandstructure materials is an essential aspect of understanding material properties and optimizing them towards relevant applications [1-4]. A crucial element of this is the extraction of the scattering relaxation times that determine electronic transport, and their energy-, momentum- and band-dependence complexities [5-11]. In the absence of efficient and reliable tools to account for these, the majority of thermoelectric studies, for example, smear all these dependencies into a single number, typically $\tau = 10$ fs, referred to as the constant relaxation time approximation (CRTA) [12, 13]. State of the art first principles methods account for all scattering complexities by calculating billions of the matrix elements that contribute to the scattering rates [14-19], but this makes them computationally extremely expensive, especially for 3D systems, [20] inflexible in accounting for all major scattering mechanisms, and thus rarely used for such studies.

The *ElecTra* simulator addresses the challenge of electronic and thermoelectric transport in complex bandstructure materials by solving the linearized Boltzmann transport equation (BTE) for charge transport in the relaxation time approximation. By using deformation potential theory and wave-vector and energy-dependent momentum relaxation times, *ElecTra* computes transport in a reliable and computationally attractive way, constituting the middle ground between the CRTA and fully *ab initio* scattering rate calculations. *ElecTra* considers the first-order solution of the BTE, [21, 22] and computes the charge transport coefficients by considering charge carrier scattering with phonons, ionized dopants, and alloy scattering, [5, 9, 21, 22] including bipolar effects.[23,24] *ElecTra* takes as input the electronic bandstructure and scattering parameters, forms constant energy surfaces and scattering rate expressions, and returns the charge transport coefficients electrical conductivity (σ), Seebeck coefficient (S), thermoelectric power factor ($PF = \sigma S^2$), and electronic part of the thermal conductivity (κ_e) as function of Fermi level (E_F) position and temperature (T). Output results for the CRTA and constant mean-free-path considerations are also included. Finally, special attention is placed on user-friendliness, with well-defined input/output (I/O) files, GUI interfaces, and a detailed manual that accompanies the code for execution instructions.

The manuscript is organized as follows: In Section 2 we describe the theory behind the linearized BTE formalism used. In Section 3 we describe the way that we map the electronic structure onto constant-energy surfaces, as well as the method validation with analytically known solutions and other existing codes. In Section 4 we describe the calculation of the scattering rates. Finally, Section 5 presents illustrative example cases for comparison of *ElecTra* results and outputs to those of existing codes and known semiconductors. The paper is accompanied with two Appendices. Appendix A shows the process and results for 2D materials. Appendix B contains examples of graphical user

interfaces (GUI) for using the code as an app, as well as code examples to execute the code using text files and scripts instead of app GUIs.

2. Linearized Boltzmann Transport Equation (BTE) formalism

The transport (and TE) coefficients are computed using the transport distribution function (TDF) within the Linearized Boltzmann Transport equation as rank-2 tensors in the form [7, 9, 22]:

$$\sigma_{ij(E_F, T)} = q_0^2 \int_E \Xi_{ij}(E) \left(-\frac{\partial f_0}{\partial E} \right) dE, \quad (1a)$$

$$S_{ij(E_F, T)} = \frac{q_0 k_B}{\sigma_{ij}} \int_E \Xi_{ij}(E) \left(-\frac{\partial f_0}{\partial E} \right) \frac{E - E_F}{k_B T} dE, \quad (1b)$$

$$\kappa_{eij} = \frac{1}{T} \int_E \Xi_{ij}(E) \left(-\frac{\partial f_0}{\partial E} \right) (E - E_F)^2 dE - \sigma S^2 T \quad (1c)$$

where $\Xi_{ij}(E)$ is the Transport Distribution Function (TDF) defined below in Eq. (2), E_F , T , q_0 , k_B , and f_0 , are the Fermi level, absolute temperature, electronic charge, Boltzmann constant, and equilibrium Fermi distribution, respectively.

The TDF is expressed as a surface integral over the constant energy surfaces, Ω_E^n , for each band, and then summed over the bands, as [7, 21, 22]:

$$\Xi_{ij(E, E_F, T)} = \frac{s}{(2\pi)^3} \sum_{\mathbf{k}, n} \sum_{\Omega_E^n} v_i(\mathbf{k}, n, E) v_j(\mathbf{k}, n, E) \tau_{i(\mathbf{k}, n, E, E_F, T)} \frac{dA_{\mathbf{k}_{\Omega_E^n}}}{|\bar{\mathbf{v}}(\mathbf{k}, n, E)|} \quad (2)$$

where $\mathbf{k}_{\Omega_E^n}$ represents a state on the surface Ω_E^n and $dA_{\mathbf{k}_{\Omega_E^n}}$ is its corresponding surface area element, computed as explained below in Section 3 [21]. $v_i(\mathbf{k}, n, E)$ is the i -component of the band velocity of the transport state, $\tau_{i(\mathbf{k}, n, E)}$ is its momentum relaxation time (combining the relaxation times of each scattering mechanism using Matthiessen's rule), $\frac{dA_{(\mathbf{k}, n, E)}}{|\bar{\mathbf{v}}(\mathbf{k}, n, E)|}$ is its density-of-states (DOS) [21], and s is the spin degeneracy. In the code $s = 2$ is used when the two spin sub-bands are degenerate, i.e. the material is non-ferromagnetic, but only one spin is resolved in the bandstructure, thus each band needs to account for both spins. In this case the user must enter that the bands are not spin-resolved, which is the case when spin-orbit coupling (SOC) is not considered or, for a non-ferromagnetic material, when SOC is considered in DFT, but the identical bands are removed from the full computed bandstructure. This step can be done when the bandstructure in .bxsf format is imported.

The TE coefficients are computed for each considered scattering mechanism separately, and the they are combined using Matthiessen's rule. The overall energy-dependent relaxation time τ and mean-free-path (mfp) λ are computed as well, both per-band, per scattering mechanism, and overall for all mechanisms. These are computed as:

$$\lambda_{i(E,E_F,T)} = \frac{\sum_{k,n}^{g_E^n} |v_{i(k,n,E)} \tau_{i(k,n,E,E_F,T)}| \text{DOS}_{(k,n,E)}}{\sum_{k,n}^{g_E^n} \text{DOS}_{(k,n,E)}} \quad (3a)$$

$$\tau_{i(E,E_F,T)} = \frac{\sum_{k,n}^{g_E^n} \tau_{i(k,n,E,E_F,T)} \text{DOS}_{(k,n,E)}}{\sum_{k,n}^{g_E^n} \text{DOS}_{(k,n,E)}} \quad (3b).$$

3. Electronic structure quantities

The workflow of *ElecTra* is shown in **Figure 1**. The electronic structure is entered as an input and it consists of a four-dimensional matrix (three-dimensional matrix for a 2D system) where the first three indexes are the space coordinates and the fourth is the band index. Because DFT codes usually use different formats, *ElecTra*'s interface can take as input a .bxsf format file [25, 26] enabling it to interface with any DFT code that provides the electronic structure data in this format. The code also checks the ‘completeness’ of the entered input instructions related for example to scattering mechanisms, Fermi levels, temperature ranges, and others as detailed in Appendix B (e.g. whether each phonon process is supplied its deformation potentials and its required parameters). The code then starts the construction of the constant energy surfaces that will later form the density of states (DOS) in energy by mapping the $E(\mathbf{k})$ bandstructure into a $\mathbf{k}(E)$ one. At this level, the code computes also band-related properties such as the DOS and the band velocities, separately for each band, as well as comprehensive. Then, the code checks for the consistency between the scattering parameters and the input instructions and computes the scattering related quantities and the transport coefficients.

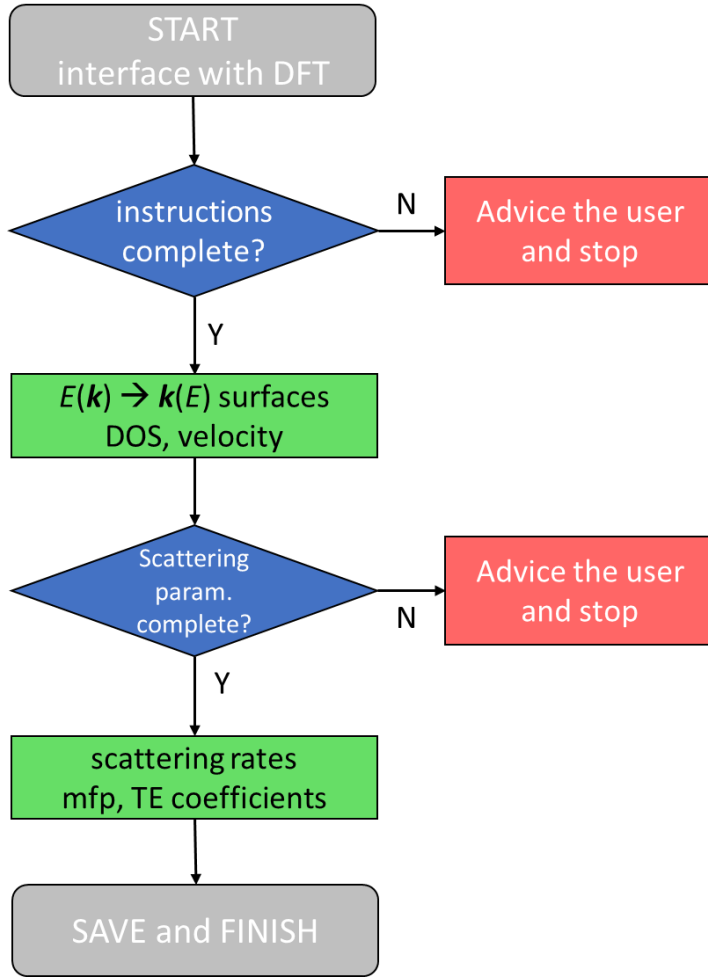


Figure 1: *ElecTra* workflow. At the beginning *ElecTra* interfaces with the output of the DFT codes to obtain the bandstructure; then, after a check of the entered calculation instructions the constant energy surfaces are built. After this, the entered scattering parameters are checked, the scattering rates are computed, the energy dependent quantities are composed, and the TDF is integrated to obtain the TE coefficients. A file containing all the data is finally saved.

To map the $E(\mathbf{k})$ into a $\mathbf{k}(E)$, the 3D mesh in the \mathbf{k} -space is scanned, the mesh elements crossed by the constant energy surfaces are identified and the coordinates of the points on these surfaces are computed. *ElecTra* offers two possibilities: i) A triangulation performed locally on the \mathbf{k} -space mesh elements which are crossed by the surface of the constant energy of interest, by dividing it into six tetrahedral as shown in **Figure 2a**. Each of them can be crossed by the constant energy surface under consideration in two ways as shown in **Figure 2b-c**. ii) An easier approximate method which uses sampling of the nearest neighbour points on the \mathbf{k} -mesh. Although the latter is an approximation because it detects only the points along the edges of the \mathbf{k} -mesh elements, it is around 15 to 30 times faster, but without noticeable penalty in the results compared to the triangulation. The discrepancies in terms of density of states (DOS) are for isotropic bandstructures at the level of the numerical noise, while for anisotropic bands the differences increase from negligible at the band edge to $\sim 1\%$ around

0.2 eV from the band edge and to $\sim 4\%$ around 0.5 eV from the band edge. Details for the two methods are provided below.

Once a mesh element is identified, the three components of the band velocity $v_{i(k,n,E)}$ are computed with the contragradient method, suitable for the arbitrary symmetry of the BZ and its 3D k -space mesh. [27] For the coordinates of the points, the $E(\mathbf{k})$ is approximated to be linear between two points “v1” and “v2” of the k -mesh, which are taken as the vertexes of the element in **Figure 2b**, or the dots on the corners in **Figure 2d**. Thus, a k_i -point at energy E_i between the vertexes v1 and v2 is selected as [28]:

$$\mathbf{k}_i = \mathbf{k}_{v1} + (\mathbf{k}_{v2} - \mathbf{k}_{v1}) \frac{E_i - E_{v1}}{E_{v2} - E_{v1}} \quad (4).$$

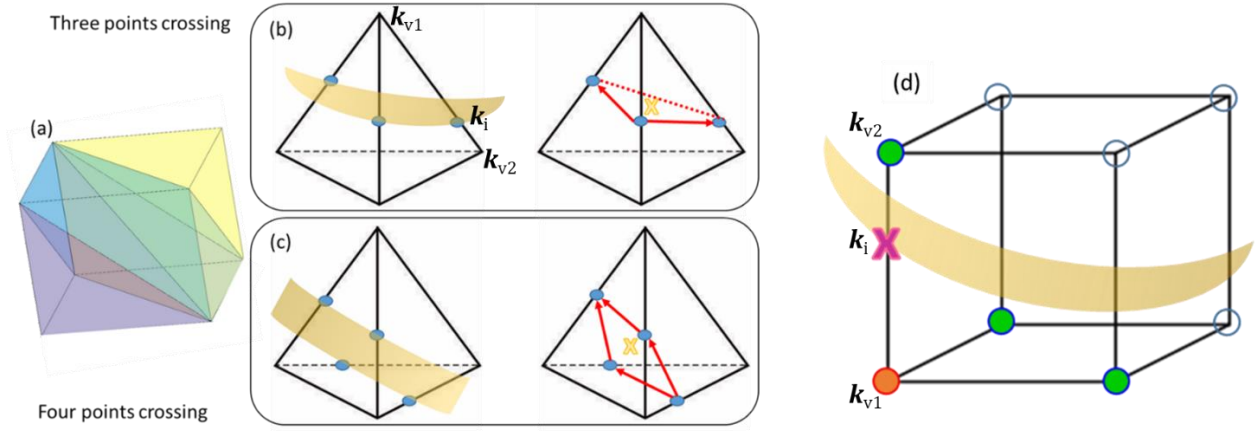


Figure 2: (a) Triangulation of a 3D mesh element. (b) and (c) show the cases where the constant energy surface of interest crosses a tetrahedron in three points (b) or four points (c). A part of the energy surface is depicted in yellow and the crossing points in blue. The surface element will be the area of the triangle in (b) or the parallelogram in (c) defined by the red arrows. Its associated element coordinates are represented by the coordinates of the barycentre shown by the yellow cross. (d) Conceptual scheme of the nearest-neighbours sampling. A k -point in a 3D k -mesh element (orange) with some of its nearest neighbours (in green). When a constant energy surface (yellow) crosses the edge between the point under consideration and its neighbour, the crossing point (purple) is selected.

Triangulation: When the triangulation method is adopted, each tetrahedron will have three (**Figure 2b**), or four (**Figure 2c**), crossing points depending on how the energy surface crosses it. These points then define a surface whose area is computed with Heron’s formula as $A = \sqrt{s_p(s_p - l_1)(s_p - l_2)(s_p - l_3)}$, where A is the triangle area, s_p is the semi-perimeter and l_i are the triangle sides. When the tetrahedron has four points, the surface element is twice the average of the areas of the four defined triangles. Such surfaces are the surface area elements $dA_{(k,n,E)}$ defining the k -state-dependent DOS, $\frac{dA_{(k,n,E)}}{|\vec{v}_{(k,n,E)}|}$, and used in the scattering rate calculations as well as the energy integrations. To obtain the k -state coordinates, which is important for anisotropic scattering rates, for

which the exchange vector is needed, the code finds the barycentre of the surface element, and labels this as the \mathbf{k} -point associated to the given surface element.

Nearest-neighbour sampling method: When the nearest-neighbour sampling method is chosen, the code scans all the \mathbf{k} -points on the energy surface and checks for their nearest neighbours along the edges of the \mathbf{k} -mesh. If the \mathbf{k} -point of interest and a neighbour have energies one above and one below the energy value of interest, the code selects a new \mathbf{k} -point along the edge of the \mathbf{k} -mesh element (**Figure 2d**), as in Eq. (4). This new point becomes the \mathbf{k} -point at the energy of interest for the scattering rate evaluation. In this way the code does not resolve a constant energy surface element but acquires a collection of points on the energy surface of interest. Then, the code assigns an effective dA_k surface element area value to each point to allow the extraction of the density of states associated with that \mathbf{k} -point. For this, all the points on the constant energy surfaces are grouped as a cloud of points. The space in the neighbourhood of each \mathbf{k} -point is explored to detect its neighbours on the surface. This is done in a radius of $1.25\sqrt[3]{V^*}$. Here V^* is the effective volume associated with the \mathbf{k} -mesh element computed as the average of the absolute values of each volume V_e used in the contragradient method, i.e. $V_e = \mathbf{k}_{lm} \cdot (\mathbf{k}_{ln} \times \mathbf{k}_{mn})$, $\mathbf{k}_{lm} = (\mathbf{k}_l - \mathbf{k}_m)$ and l, m, n , are the vertexes of the considered mesh element. $\sqrt[3]{V^*}$ is regarded as the effective distance between adjacent points in the \mathbf{k} -mesh used in the bandstructure calculation if the mesh is cubic. Then, the code calculates the average distance between the given point and its detected neighbours, $\langle \Delta k \rangle$. The surface element associated to the \mathbf{k} -point is approximated by a circle of radius half the average distance to the neighbouring points, i.e., $dA_k = \pi \left(\frac{\langle \Delta k \rangle}{2} \right)^2$. Note that the assumption of a circular region and the value of 1.25 is determined empirically here to provide the best map between the DOS of this method and the DOS of the triangulation method, and works adequately for 3D and 2D. Essentially, it indicates that the effective radius of a point to its neighbours needs to be somewhat more than its half distance in order to include points that are placed in the diagonal direction of the grid in relation to the considered point.

For each band in the electronic structure, the energy-dependent DOS is then calculated as:

$$\text{DOS}(E, n) = \oint_{\Omega_E^n} \frac{dA(\mathbf{k}, n, E)}{|\vec{v}(\mathbf{k}, n, E)|} = \frac{s}{(2\pi)^3} \sum_{\mathbf{k}_{E,n}} \frac{dA(\mathbf{k}, n, E)}{|\vec{v}(\mathbf{k}, n, E)|} \quad (5)$$

where s is the spin degeneracy taken as 1 or 2, and $\vec{v}(\mathbf{k}, n, E)$ is the band velocity. The comprehensive DOS(E) is the sum of the DOS of all individual bands and the comprehensive velocity $v(E)$ is the average of the state velocity $v(E, n) = \langle |\vec{v}(\mathbf{k}, n, E)| \rangle_{\mathbf{k}}$.

The implementation of these concepts in *ElecTra* are shown in **Figure 3** for three example cases: (i) parabolic bands, where the analytical solution is known, (ii) the valence band of the half-Heusler TiCoSb, and (iii) the conduction band of Mg₃Sb₂. **Figure 3a-c** shows an example of constant energy

surfaces together with 1D projections of the bandstructures, with the magenta lines indicating the energy of the surfaces. In **Figure 3d** the DOS of an isotropic parabolic band with mass equal to the rest mass of the electron, m_0 , is shown, depicting in blue the analytical solution $DOS(E) = \frac{\sqrt{2}}{\pi^2 \hbar^3} m^{3/2} \sqrt{E}$, in orange the values computed by *ElecTra* with the nearest-neighbour sampling method and in green with the triangulation method. In the same sub-figure we also show the cases for an anisotropic non-parabolic band, following the same colouring scheme (bottom lines). For this case the three masses along the three coordinate directions are 1, 0.5, 0.1, in units of m_0 , and the non-parabolicity coefficient is $\alpha = 0.5/q_0 \text{ eV}^{-1}$, with q_0 being the electron charge. The analytical DOS in this case is $DOS(E) = \frac{\sqrt{2}}{\pi^2 \hbar^3} m_D^{3/2} (1 + 2\alpha E) \sqrt{E(1 + \alpha E)}$ with $m_D = \sqrt[3]{m_x m_y m_z}$. **Figure 3e** reports the band velocity for these two cases, with the isotropic parabolic band corresponding to the bottom lines, following the analytical solution $v(E) = \sqrt{2E/m}$. The anisotropic non-parabolic band case corresponds to the top lines, with analytical solution $v(E) = \frac{\sqrt{2E(1+\alpha E)/m_c}}{\sqrt{1+4\alpha E(1+\alpha E)}}$ with $m_c = \frac{3}{\sum_i 1/m_i}$. Excellent agreement between analytical and numerical calculations is observed. **Figure 3f** shows the total DOS for the TiCoSb valence band computed with Quantum Espresso [29, 30] in blue, and with *ElecTra* in orange and green using nearest-neighbour sampling and triangulation, respectively. An excellent agreement between *ElecTra* and Quantum Espresso is observed. The corresponding band velocity is shown in **Figure 3g**. The comparison between *ElecTra* and BoltzTraP [12] is shown in **Figure 3h** for the Mg₃Sb₂ conduction band, whereas the corresponding band velocity is reported in **Figure 3i**. Again, excellent agreement between *ElecTra* and BoltzTraP is observed. Some minor differences are likely because *ElecTra* considers constant energy surfaces and surface integrals instead of fixed k -points and volume integrals.

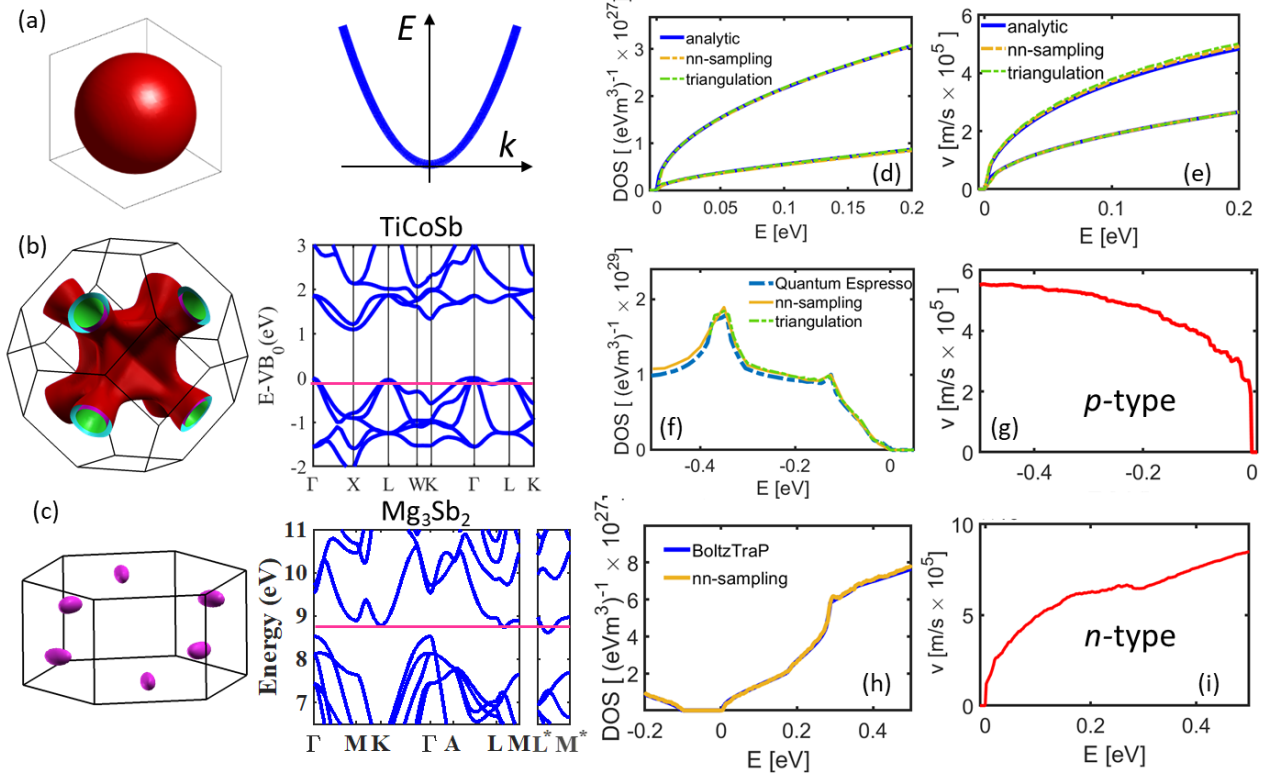


Figure 3: (a) Constant energy surface (sphere) for an isotropic parabolic band. (b) Constant energy surface for the valence band of TiCoSb, 0.12 eV below the valence band edge. (c) Constant energy surface for the Mg₃Sb₂ conduction band, 0.1 eV above the edge. (d) 3D DOS for isotropic parabolic band ($m^* = m_0$ – top lines), case (a), and anisotropic non-parabolic band ($m_{x,y,z}^* = 1, 0.5, 0.1 m_0$ and $\alpha = 0.5$ – bottom lines); comparison of the known analytical solution with the one numerically computed with *ElecTra*, by using the two sampling schemes for the BZ. (e) Band velocity for the case in (d), top lines for anisotropic non-parabolic band and bottom lines for isotropic parabolic. (f) DOS for the TiCoSb (Zincblende structure) valence band, comparison of the results from Quantum Espresso with those from *ElecTra*. (g) Band velocity for the TiCoSb valence band. (h) DOS for the Mg₃Sb₂ conduction band, comparison between the results from BoltzTraP and *ElecTra*. (i) Band velocity for the Mg₃Sb₂ conduction band.

4. Carrier scattering and transport quantities

For each transport state (\mathbf{k}, n, E) and each scattering mechanism m_s , the corresponding relaxation time $\tau_{i(\mathbf{k}, n, E)}^{(m_s)}$ is defined as:

$$\frac{1}{\tau_{i(\mathbf{k}, n, E)}^{(m_s)}} = \frac{1}{(2\pi)^3} \sum_{\mathbf{k}'} |S_{\mathbf{k}, \mathbf{k}'}^{(m_s)}| \left(1 - \frac{v_{i(\mathbf{k}')}}{v_{i(\mathbf{k}, n, E)}} \right) \quad (6)$$

where the sum runs over all the allowed final states \mathbf{k}' of the same carrier spin. [21, 22] $|S_{\mathbf{k}, \mathbf{k}'}|$ is the transition rate between the initial \mathbf{k} and final \mathbf{k}' states, computed as detailed by Eq. 7 below for the different mechanisms. The $\left(1 - \frac{v_{ij(\mathbf{k}')}}{v_{ij(\mathbf{k}, n, E)}} \right)$ term is an approximation for the momentum relaxation time, [31-34] which is the type of relaxation time that matters when computing the transport

coefficients. [21] *ElectTra* computes the scattering rates using Fermi's Golden Rule for the different scattering mechanisms as (for 3D materials, see Appendix for the 2D versions) [21, 22]:

$$|S_{\mathbf{k},\mathbf{k}'}^{(ADP)}| = 2 \frac{\pi}{\hbar} D_{ADP}^2 \frac{k_B T}{\rho v_s^2} g_{\mathbf{k}'} \quad (7a)$$

$$|S_{\mathbf{k},\mathbf{k}'}^{(ODP)}| = \frac{\pi D_{ODP}^2}{\rho \omega} \left(N_\omega + \frac{1}{2} \mp \frac{1}{2} \right) g_{\mathbf{k}'} \quad (7b)$$

$$|S_{\mathbf{k},\mathbf{k}'}^{(IVS)}| = \frac{\pi D_{IVS}^2}{\rho \omega} \left(N_\omega + \frac{1}{2} \mp \frac{1}{2} \right) g_{\mathbf{k}'} \quad (7c)$$

$$|S_{\mathbf{k},\mathbf{k}'}^{(POP)}| = \frac{\pi q_0^2 \omega}{|k-k'|^2 \varepsilon_0} \left(\frac{1}{k_\infty} - \frac{1}{k_s} \right) \left(N_{\omega, BE} + \frac{1}{2} \mp \frac{1}{2} \right) g_{\mathbf{k}'} \quad (7d)$$

$$|S_{\mathbf{k},\mathbf{k}'}^{(IIS)}| = \frac{2\pi}{\hbar} \frac{Z^2 q_0^4}{k_s^2 \varepsilon_0^2} \frac{N_{imp}}{\left(|k-k'|^2 + \frac{1}{L_D^2} \right)^2} g_{\mathbf{k}'} \quad (7e)$$

$$|S_{\mathbf{k},\mathbf{k}'}^{(Alloy)}| = \frac{2\pi}{\hbar} \Omega_c \chi (1-x) G_{(k-k')} \Delta E_G^2 g_{\mathbf{k}'} \quad (7f)$$

Above, ADP stands for ‘Acoustic Deformation Potential’ and represents the scattering between charge carriers and acoustic phonons. ODP stands for ‘Optical Deformation Potential’ and describes the charge carrier inelastic scattering with non-polar optical phonons. Both can be chosen to be both intra- and/or inter-*band* (in subsequent versions of the code we will allow for the choice of intra- versus inter-*valley* scattering as well). IVS stands for ‘Inter-Valley Scattering’ and it is specific for the inelastic inter-valley scattering. POP stands for ‘Polar Optical Phonon’ and describes the inelastic/anisotropic scattering of charge carriers with polar phonons, which here is treated as both intra- and inter-band [22]. IIS stands for ‘Ionized Impurity Scattering’ and describes the elastic scattering rate due to ionized dopants, for which the user can choose both intra- and/or inter-band nature for transitions. ‘Alloy’ represents the alloy scattering due to intrinsic disorder in alloys or solid solutions and is both intra- and inter-band. [31] \mathbf{k} and \mathbf{k}' are the wave vectors of the initial and final states. ‘-’ and ‘+’ in Eqs. 7b-7d indicate the phonon absorption and emission processes, respectively. Examples for these types of transition processes are depicted in **Figure 4a**.

The variables that appear in Eq. 7 are as follows: D_{ADP} , D_{ODP} , D_{IVS} are the deformation potentials for the ADP, ODP, and IVS mechanisms. ρ is the mass density, v_s the sound velocity, ω the dominant frequency of optical phonons, considered as constant over the whole reciprocal unit cell, which has been validated to be a satisfactory approximation, [15] and N_ω is the phonon Bose-Einstein statistical distribution; ε_0 the vacuum dielectric constant, k_s and k_∞ the static and high frequency relative permittivity, Z the electric charge of the ionized impurity considered, and N_{imp} is the density of the ionized impurities. $g_{\mathbf{k}'} = \frac{dA_{(k',n,E)}}{|\bar{v}_{(k',n,E)}|}$ is the single-spin DOS of the final scattering state. $L_D =$

$\sqrt{\frac{k_s \varepsilon_0}{e} \left(\frac{\partial n}{\partial E_F} \right)^{-1}}$ is the generalized screening length with E_F being the Fermi level and n the carrier

density. [22, 9] Ω_c is the volume of the primitive cell, x the fraction of one of the alloy elements, G is the for factor of the hard sphere, [31] and ΔE_G the difference between the energy gap of the two constituent materials that form the alloy. [22, 31] Rigorous studies show that the ΔE_G can be substituted by an effective scattering potential that can be calibrated to fit experimental values. [31] However, *ElecTra* uses the ΔE_G term, since in general such scattering potentials are unknown.

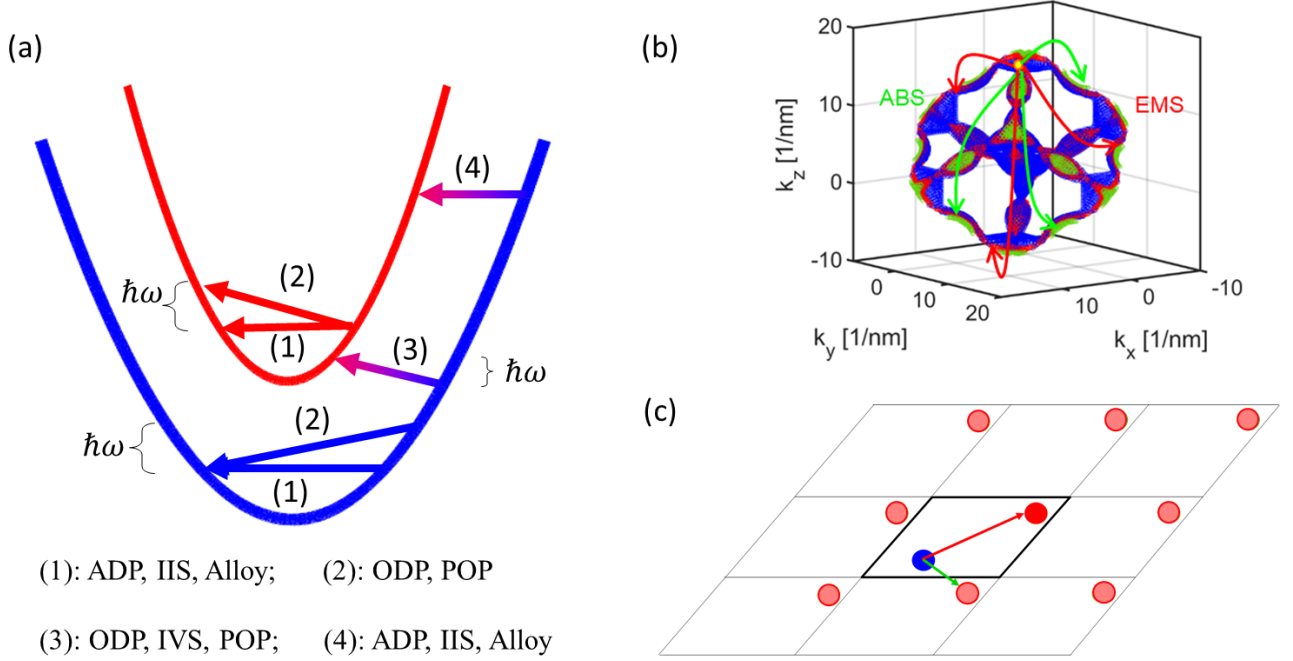


Figure 4: (a) Schematic of two bands with the four types of allowed transitions: (1) elastic intra-band; (2) inelastic intra-band, (3) inelastic inter-band, (4) elastic inter-band. $\hbar\omega$ is the energy of the absorbed or emitted phonon. (b) The same iso-energy surface as in **Figure 1b**, in blue, with transport state representation – each point is a transport state. Two other iso-energy surfaces (green/red) from another valence band and at different energies are depicted with relative arrows to signify absorption/emission transitions, indicated as ABS and EMS. To compute the tensor components of the TE coefficients, *ElecTra* expresses the surfaces, from DFT calculation on the BZ, in Cartesian axes. (c) 2D schematic of the reciprocal unit cell used in the calculation, with bold edges, and its equivalent cells around it. The initial k-point is in blue and the final k-point in red. The equivalent final k-points are shown in faded red, obtained by translating the red point by one reciprocal lattice vector in all possible directions. In the anisotropic POP and IIS scattering mechanisms, all the equivalent k-points are explored, and the final k-point considered is the one closest to the initial k-point. This is used for the $|k-k'|$ term and for charge screening (IIS and POP).

The current version of *ElecTra* (v1) is calibrated towards the predictive modelling of electronic and thermoelectric properties of materials and it is validated to room and higher temperatures. It considers that all dopants are ionized and does not capture the carrier freeze out region. Note that the equipartition theorem at the basis of Eq. 7a does not hold at low temperatures either. Screening in the electron-phonon scattering processes is implemented only for the POP mechanism, where it is believed to play a major role, [35-38] for which the user has the choice to include the screening factor

$\frac{1}{\left(1 + \frac{1}{|k-k'|^2 L_D^2}\right)^2}$ in the calculation. [22, 39] The screening in the carrier-phonon scattering event has

different effect on transport depending on the bandstructure details. It has little effect for light bands with small ellipsoids and small DOS (larger L_D) such as in GaAs, the difference in mobility is below 5 % and concentrated in the low doping regime, and greater effect for bands with large constant energy surfaces and large DOS (smaller L_D) such as the valence bands of half-Heuslers, where the difference in the mobility can be ~ 50 % and extended in a wider doping interval. However, it substantially increases the computational complexity (as the scattering rates become Fermi level dependent), so its consideration is left to the user's choice.

The scattering rates and the transport coefficients are computed along orthogonal Cartesian space directions x, y, z . Consequently, the constant energy surfaces are expressed in Cartesian coordinates on orthogonal axes instead of unit cell axes, and the reciprocal unit cell is used instead of the Brillouin Zone. The surfaces in **Figure 3b**, represented as a collection of transport states in Cartesian coordinates, are depicted in **Figure 4b**. The process of carrier scattering is depicted by arrows between points (i.e. transport states) either on same or different energy surfaces (resembling elastic/inelastic processes).

A further important point is that the POP and IIS scattering strengths depend on the momentum exchange vector, i.e. the distance in the k -space between the initial and final states $|\mathbf{k} - \mathbf{k}'|^2$. To compute this momentum exchange vector, the simulator takes into consideration every final state's k -point position in all neighbouring reciprocal unit cells, and then uses the minimum distance from the initial point in the exchange vector. For this, as shown in a 2D schematic in **Figure 4c**, the final point (red bullet), is shifted by the reciprocal lattice vectors in all possible directions, creating the fainted red bullet points. Here in **Figure 4c** the central cell with bold edges represents the cell used in the simulations and the other cells are the equivalent ones. Then the code considers the closest distant to the initial blue bullet point. This is necessary, because for example two k -points that are located at opposite edges of the reciprocal unit cell are actually very near if the equivalent point in the nearest neighbour cell is considered. **Figure 4c** shows a 2D schematic of this, indicating that the physical scattering vector is the green one, and not the red one.

Illustrative examples for transport quantities – case of parabolic bands: We now show some illustrative examples of the energy dependent quantities computed by *ElecTra*. We consider the relaxation times τ , mean-free-paths λ , and transport distribution functions \mathcal{E} , and first compare parabolic bands (with known analytical solutions). We then consider the valence band of TiCoSb as a case study. In **Figures 5a-d** we show the relaxation time and mean-free-path (mfp) computed for

an isotropic parabolic band with $m = m_0$, under different scattering mechanisms as detailed in the figure. In addition to the scattering parameters detailed in the caption, we assumed a mass density of 9 g/cm^3 , speed of sound 3 km/s , and static and high-frequency dielectric constants of 12 and 10. We consider room temperature $T = 300 \text{ K}$. The behaviour is the typical one described in the literature [21]. In **Figure 5a** the relaxation time due to ADP decreases with energy due to the increasing DOS. The same generally holds for ODP with the additional consideration that at the band edge only phonon absorption is possible. When phonon emission becomes possible, the relaxation time drops down as expected. **Figure 5a** also shows the relaxation time for scattering with ionized impurity scattering at a dopant density of $2 \times 10^{19} \text{ cm}^{-3}$, which corresponds to a Fermi level at the band edge. It also shows the total relaxation time by combining ADP, ODP and IIS according to Matthiessen's rule. In **Figure 5b** we show the mean-free-path, λ , for three of the situations of **Figure 5a**, for the parabolic bands. Namely, the mfps are: i) a roughly constant under ADP, ii) initially increasing under ODP when only absorption is possible, then decreasing and settling to a nearly constant value, and iii) following an increasing trend under IIS, which is the strongest for carriers at the band edge, such that λ tends to get closer to the phonon-limited value at higher energies. We show POP separately in **Figures 5c-d**, specifically differentiating the role of screening which can be included for this scattering mechanism. **Figures 5c** and **5d** show the relaxation time and mean-free-path, respectively, for the case where carrier screening is *not* included in the POP scattering calculation (blue lines), and when it *is* included (magenta lines). The three magenta lines show how these quantities vary for different carrier densities as indicated in **Figure 5d**. For non-degenerate conditions the effect is negligible, while it becomes sizeable at degenerate conditions by weakening the scattering strength by a factor of around 2 to 3.

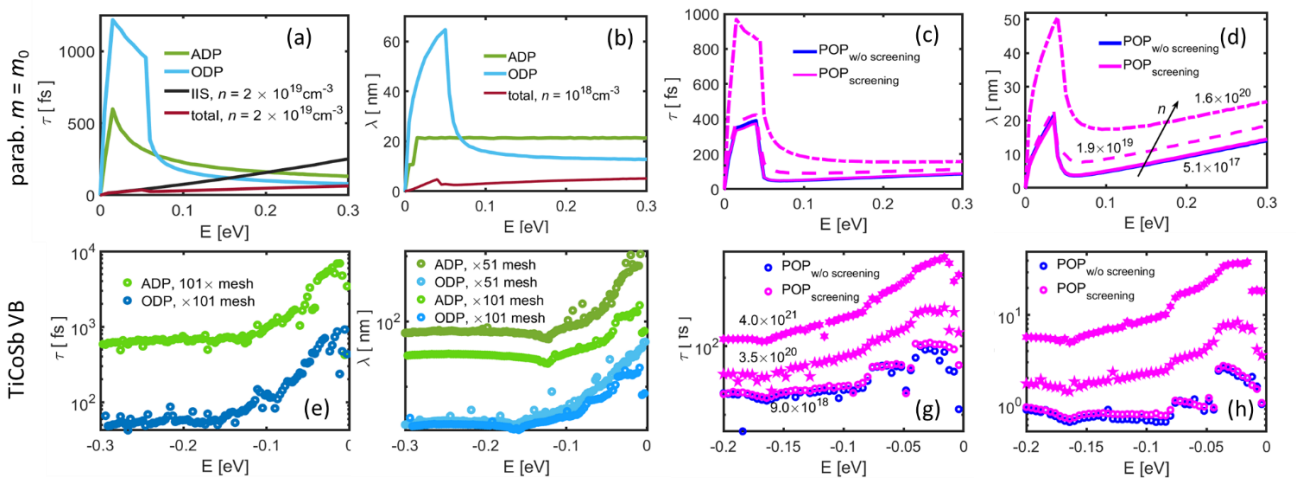


Figure 5: *ElecTra* simulation examples for: (a) Scattering times and (b) mean-free-paths for ADP (10 eV) and ODP (5×10^{10} eV/m, phonon energy 50 meV) mechanisms in an isotropic parabolic band ($m = m_0$). (c) and (d) are the same as (a) and (b) for the POP mechanisms (phonon energy 40 meV), without (blue) and with (magenta) charge screening. In the latter case, the rates depend on the doping level. (e) Scattering times and (f) mean-free-paths for TiCoSb valence band for the ADP and ODP mechanisms. In (f) two k -mesh densities are compared. (g)-(h), same as (c)-(d) but for the TiCoSb valence band.

Illustrative examples for realistic materials – the case of TiCoSb: We now show the cases of relaxation times and mean-free-paths for the half-Heusler TiCoSb in **Figure 5e-h**, with the scattering parameters used taken from ref. [9]. Illustrative bandstructure figures are shown in **Figure 3(b)**. We start with ADP and ODP in **Figure 5e-f**. Note that the valence bands are in the negative energy direction and the band edge at 0eV, so the lines should be read from right to left. For both cases we have the rise of τ and λ at the band edge and reduction further into the bands, however, these raises are disguised by the numerical DOS which is highly non parabolic (**Figure 3f**). In **Figure 5f** we also compare the effect of the mesh size, by employing two regular meshes of 51 points and 101 points along each k -space coordinate direction, respectively. A finer mesh, despite taking longer time, strongly reduces the numerical noise. The computation time is ~ 25 min. and increases to ~ 9 hrs when the mesh increases from 51 to 101 k -points meshes, when *ElecTra* is parallelized on a 12 CPUs desktop PC.

In **Figures 5g-h**, we show the relaxation time and mean-free-path due to POP with and without screening. The blue lines correspond to the cases without screening, whereas the magenta lines for the cases of three carrier densities as above in **Figures 5c-d**. For TiCoSb, the dielectric constant values assumed in the POP calculations are 30 and 20 for the static and high frequency, respectively [40]. As in the case of parabolic bands, the screening effect is negligible at low densities, but here it becomes very strong at increased carrier densities, leading to a variation of more than an order of magnitude. The valence band of TiCoSb is strongly non-parabolic with wide energy surfaces. This leads to higher carrier density (and screening lengths) and especially wider exchange vectors, two factors which strongly increase carrier screening and increase scattering times and mfp (much more compared to the parabolic band cases).

TDF illustrative examples: We now show examples of transport distribution functions (TDF) \mathcal{E} , which contain all the information relevant to charge transport within the BTE. We first show examples of these functions for different scattering mechanisms in the case of parabolic bands. In **Figure 6a** we show \mathcal{E} for the same parabolic band as in **Figures 5a-d**, for the three electron-phonon scattering mechanisms computed with *ElecTra*. As expected, ADP gives a linear \mathcal{E} in the parabolic band case, while for ODP and POP the onset of the phonon emission at the characteristic phonon

energy is clearly observed (here we used 50 meV for ODP and 40 meV for POP). Also, the effect of the anisotropic character of the POP scattering is noticeable, with higher than linear increase of \mathcal{E} , for the high energy, large exchange vector, carriers. In **Figure 6b** we compare the two \mathcal{E} functions for ODP and POP from **Figure 6a** to the known analytical solutions, showing once again the validity and reliability of the *ElecTra* numerical implementation.

In **Figure 6c** we show the corresponding TDFs for the valence band of TiCoSb to indicate how a full-band treatment of non-ideal bandstructures impacts the transport distribution functions. \mathcal{E} is no longer linear for ADP, and the abrupt jump at the phonon emission onset in ODP is mitigated (as observed in the logarithmic and linear-inset scales). Note that the assumed optical phonon frequency is 36 meV and that the figures need to be read from right to left. It is the DOS which seems to have a strong influence on the \mathcal{E} features. [5] In **Figure 6d** we show \mathcal{E} computed when considering all ADP, ODP and IIS altogether, and for three carrier densities, showing that an increasing dominant IIS tends to smear out some of the DOS features, although the more than linear trend expected from parabolic bands is absent – the trend here is rather linear. Note that the scattering parameters for TiCoSb are the same as used in ref. [9].

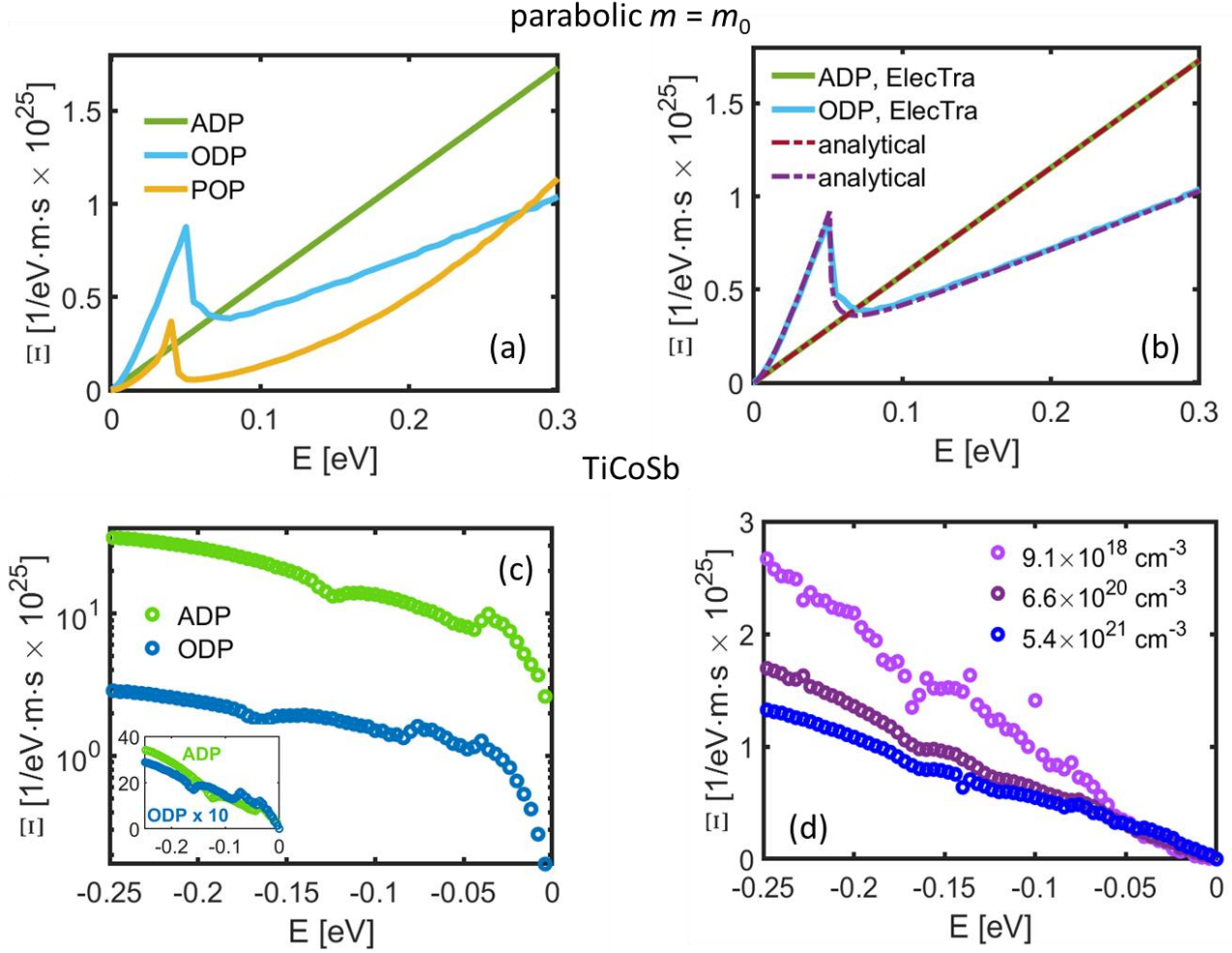


Figure 6: (a) The .xx component of the TDF for an isotropic parabolic band ($m = 0.1$) for three different scattering mechanisms, as specified in the legend. (b) Validation of two TDFs in (a) with the analytical solution. (c) The .xx component of the TDF for the TiCoSb valence band, for ADP and ODP mechanisms. The inset depicts the case for the y-axis in linear scale. (d) The total .xx component of the TDF for TiCoSb for three different hole densities as specified in the legend. For TiCoSb, the shown data are for the $101 \times 101 \times 101$ k -mesh.

5. Transport coefficient validations

Now we present the validation of the *ElecTra* simulator with comparison to BoltzTraP, a widely used simulation code that uses the constant relaxation time approximation (CRTA) [12, 13]. We also show simulations from *ElecTra* regarding the well-studied semiconductors Si, Ge, SiGe alloy, GaAs.

We start with a comparison between the TE coefficients computed under the CRTA by *ElecTra* and BoltzTraP for TiCoSb, i.e. the electrical conductivity, σ , in **Figure 7a** and the power factor, $PF = \sigma S^2$, in **Figure 7b**. A very good agreement is observed with a maximum difference of $\sim 10\%$. In **Figure 7c** we report the comparison of σ for two different tensorial components for another

thermoelectric material, Mg_3Sb_2 . Again the differences are below 10%. We also note that the mesh we used in this calculation is rather sparse, $51 \times 51 \times 51$ for TiCoSb and $61 \times 61 \times 41$ for Mg_3Sb_2 .

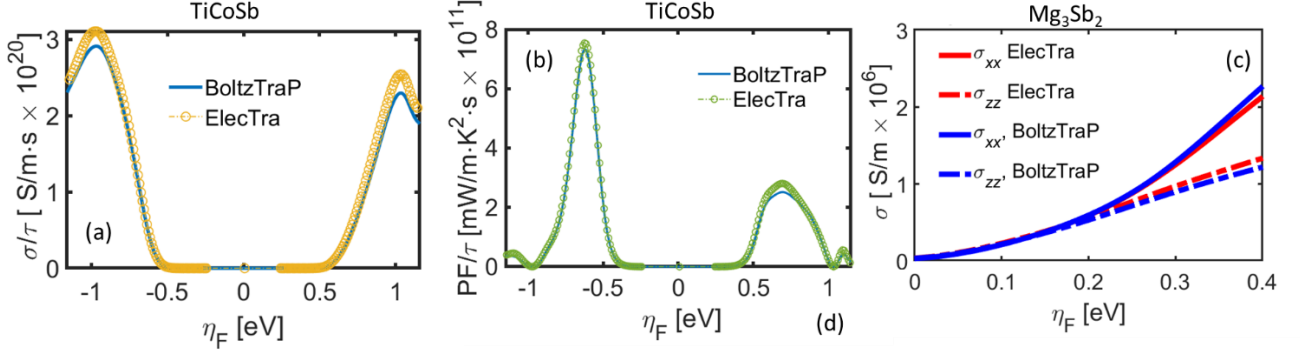


Figure 7: Validation of *ElecTra* with BoltzTraP for TiCoSb , (a) and (b), and for Mg_3Sb_2 , (c). The BoltzTraP results are in blue. The mesh used by *ElecTra* is $51 \times 51 \times 51$ for TiCoSb and $61 \times 61 \times 41$ for Mg_3Sb_2 . These are in general sparser meshes than that we would have used, but for matter of comparison between the two codes they are adequate.

We now validate *ElecTra*'s transport calculations versus experimentally well-known semiconductors by comparing the computed and experimental mobility using data from the literature. [41-45]. In **Figures 8a-b** we show the case of *n*- and *p*-type silicon mobility respectively, including ADP, ODP and IIS with the figures, parameters, and full details of the calculation adopted from [46]. The very good agreement corroborates the validity of the implemented scattering and transport methods. The discrepancies at the higher doping region can be ascribed to electron-electron scattering, [46] which is not included in the computation.

GaAs offers the possibility to further validate the *ElecTra* scattering treatment by investigating a material for which POP is dominant. In addition, two type of valleys, Γ and L, participate in transport and different deformation potentials determine the scattering strengths between them [21]. GaAs also offers the possibility of testing the relevance of the carrier screening in the POP mechanism. As we observe in **Figure 8c**, the consideration of screening in the POP mechanisms has little effect, attributed to the small effective mass of the Γ valley, which results in larger screening length and smaller exchange vectors. As seen above, POP screening becomes important at higher carrier densities, but then the IIS is dominant. However, materials with large energy surfaces such as half-Heuslers could have a different behaviour. In **Figure 8c** we also show the mobility computed without the $\left(1 - \frac{v_{ij}(k')}{v_{ij}(k,n,E)}\right)$ momentum relaxation term in Eq. (6), signalling its importance when the relevant scattering processes are anisotropic.

The case of Ge mobility is shown in **Figure 8d**, where again the *ElecTra* simulations map very well to experiments. This figure, however, also highlights the importance of the mesh spacing. Using

units of π/a , where a is the lattice parameter, a spacing of $0.01 \pi/a$ corresponds to a $201 \times 201 \times 201$ bandstructure mesh. A spacing of $0.02 \pi/a$ can be sufficient to capture the general trends in the transport properties and could be sufficient in materials screening/ranking or comparisons. However, for better quantitative accuracy, a spacing of maximum $\sim 0.015 \pi/a$ is recommended.

The case of the SiGe alloy, in **Figure 8e**, is used to validate the ‘Alloy’ scattering treatment. In this case, a low doping value of $\sim 10^{14} \text{ cm}^{-3}$ is considered. For Ge, the scattering deformation potentials are taken from reference [45], and for the SiGe alloys, they have been linearly combined, weighted by the composition. Note that in the general case, there can be different number of processes for each material and a weighted deformation potential cannot be trivially extracted. For example, with regards to IVS in silicon, there are three tabulated IVS processes [46] while there are only two for germanium [45] (for example the Si g- and f-processes are not relevant for Ge). One first order approach (not unique) to tackle this would be to determine on an arbitrary basis the deformation potentials for the minimum number of processes that however provide the elemental material mobility. Since now, both materials will be described by the same number of processes, we can combine these fictitious deformation potentials with Vegard’s law. The calculation agrees very well with the experiments; however, we acknowledge a better process needs to be identified. Finally, in **Figure 8f** we compute the mean-free-paths for some of the materials, as indicated in the figure, for both non-degenerate (dash-dot lines) and heavily degenerate conditions (solid lines), indicating the capability of *ElecTra* to provide meaningful intrinsic transport quantities.

We also highlight that *ElecTra* approach is suitable also for metals, semimetals, and gapless semiconductors. [50, 51] For zero and negative bandgaps, *ElecTra* can consider the scattering between the “valence” and “conduction” bands, which can even be the case of inelastic scattering in a semiconductor with a bandgap smaller than the phonon energy.

A final mention is regarding the overlap integrals. This is usually considered to be unity [47, 48], but there are expressions that can also be used for different cases and materials. [22] In *ElecTra* the user can choose to use, for the generic valence band material case the ones developed for silicon. [49]

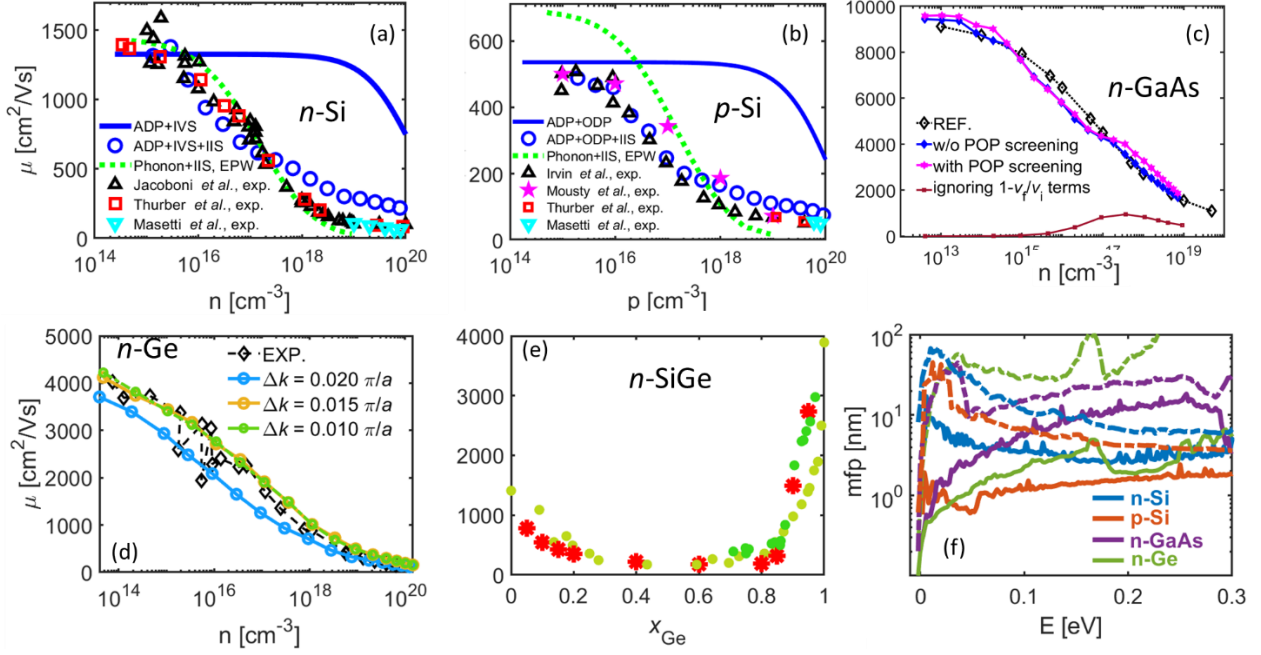


Figure 8: (a-b) Simulation versus experiment for silicon electron and hole mobility versus carrier density at 300 K. The computation for Silicon uses DFT bandstructure (with SOC) and tabulated deformation potentials (Lundstrom). (c) Simulation versus experiment for the electron mobility in GaAs; the conduction band has been numerically constructed from the nominal effective masses and non-parabolicity coefficients. (d) Simulation versus experiment for the electron mobility in Ge. Nominal parameters for the bandstructure and scattering are used. [21, 41, 42, 43, 44, 45] The effect of the spacing in the k -space is displayed. (e) SiGe low doping electron mobility, red stars are computed values whereas the green dots are experimental points. (f) mfps for (a)-(d) at low doping (dash-dot) with $E_F \sim 0.2$ eV in the gap, and at high doping (solid) with $E_F \sim 0.1$ eV into the band. (a) and (b) reproduced with permission. [46] (a-b), "Reprinted (figure8) with permission from [Z. Li, P. Graziosi, N. Neophytou, Phys. Rev. B, 104, 195201 (2021)] Copyright (2021) by the American Physical Society.

6. Conclusions

We have introduced *Electra*, a code to solve the linearized Boltzmann transport equation by considering the full energy, momentum and band index dependence of the scattering relaxation time. The code has been tested versus analytical solutions, existing codes operating under constant relaxation time approximation, and experimental data, achieving an excellent agreement. The code can offer a large degree of accuracy with a significantly reduced computational cost compared to fully ab initio methods, and can be a useful resource in computing electronic and thermoelectric transport properties in complex bandstructure materials.

Acknowledgement

This work has received funding from the Marie Skłodowska-Curie Actions under the Grant agreement ID: 788465 (GENESIS - Generic semiclassical transport simulator for new generation thermoelectric materials) and from the European Research Council (ERC) under the European Union's Horizon 2020 Research and Innovation Programme (Grant Agreement No. 678763). We acknowledge support from Dr. Chaturangi Kumarasinghe in the validation of the algorithms for the formation of the constant energy surfaces, and from Prof. Laura De Sousa Oliveira for the initial set up of the parallelization concepts. For part of the computational time, we acknowledge the CINECA award under the ISCRA initiative, for the availability of high performance computing resources and support.

Appendix A – 2D transport coefficients

In this section we present the extension of *ElecTra* to 2D materials, report the scattering rate equations, and validate this computational method. In 2D the TDF is expressed as [28]:

$$\bar{E}_{ij(E,E_F,T)} = \frac{s}{(2\pi)^2} \frac{1}{t} \sum_{\mathbf{k},n} \mathfrak{C}_E^n v_{i(\mathbf{k},n,E)} v_{j(\mathbf{k},n,E)} \tau_{i(\mathbf{k},n,E,E_F,T)} \frac{d\ell_{\mathbf{k}_{\mathfrak{C}_E^n}}}{|\bar{\mathbf{v}}_{(\mathbf{k},n,E)}|} \quad (\text{A.1}),$$

where t is the material thickness, for example the unit cell size in the vertical direction, \mathfrak{C}_E^n is the constant energy contour of band n , and $d\ell_{\mathbf{k}_{\mathfrak{C}_E^n}}$ is the corresponding length element for the $\mathbf{k}_{\mathfrak{C}_E^n}$ state, computed by reducing to two dimensions the approach described in Section 3; all other terms in Eq.

(A.1) are the same as in Eq. (2). $\frac{d\ell_{\mathbf{k}_{\mathfrak{C}_E^n}}}{|\bar{\mathbf{v}}_{(\mathbf{k},n,E)}|}$ is the k -state density-of-states. It must be noted that in 2D the triangulation and nearest-neighbour approach requires nearly the same computation time for both the $k(E)$ extraction and scattering rates calculation, so the nearest-neighbour approach does not lead to any computational cost benefits in 2D. However, both options are still available to the user. For the parabolic band example below, the computational time to build the constant energy contours is around 10 s and for scattering rates and transport coefficients around 8 minutes, in a laptop computer with 6 processors, regardless the used sampling scheme, triangulation or nearest-neighbours.

The scattering rate calculations, Eqs. (7), for all the mechanisms except POP and IIS scattering mechanisms, are generally the same. In Eqs. 7a,b,c,f, an $1/t$ multiplication is required to account for the 2D nature of the system and the correct units, i.e. the mass density is still entered in Kg/m^3 for ADP, ODP and IVS, and the 2D volume cell for Alloy is still entered in m^{-3} , and those units need to be adjusted. The POP and IIS scattering rates are computed as:

$$|S_{\mathbf{k},\mathbf{k}'}^{(POP)}| = \frac{\pi q_0^2 \omega}{2|\mathbf{k}-\mathbf{k}'|_{\varepsilon_0}} \left(\frac{1}{k_\infty} - \frac{1}{k_s} \right) \left(N_{\omega,BE} + \frac{1}{2} \mp \frac{1}{2} \right) g_{\mathbf{k}'} \quad (\text{A.2a})$$

$$|S_{\mathbf{k},\mathbf{k}'}^{(IIS)}| = \frac{\pi}{2\hbar} \frac{Z^2 q_0^4}{k_s^2 \epsilon_0^2} \frac{N_{imp}}{|\mathbf{k}-\mathbf{k}'|^2 + \frac{1}{L_D^2}} g_{\mathbf{k}'} \quad (\text{A.2b}).$$

The terms in Eq.s (A.2) are the same as in Eq.s (7) except $g_{\mathbf{k}'} = \frac{d\ell_{(\mathbf{k}',n,E)}}{|\vec{v}_{(\mathbf{k}',n,E)}|}$. The form of Eq.s (A.2) is based on the fact that the Fourier transform (FT) [21, 22] of the Coulomb-like field $\sim 1/r$ in 2D is $2\pi/q$ instead of the 3D $4\pi/q^2$, and for a screened field the FT of $\sim 1/r \exp(-L_D/r)$ is $\frac{2\pi}{\sqrt{q^2 + L_D^2}}$ in 2D instead of the 3D $\frac{4\pi}{q^2 + L_D^2}$, [52] where r is the distance from the charge. Remarkably, the comparison between Eq. (A.2a) and Eq. (7f) reflects the expressions for 3D and 2D materials in the approximation where no dielectric is assumed to be surrounding the material and absence of image charges. [53-56] Similarly, the screening term which can be eventually added to the POP scattering mechanism becomes $\frac{1}{1 + \frac{1}{|\mathbf{k}-\mathbf{k}'|^2 L_D^2}}$. Finally, the screening length in 2D is computed as $L_D = 2 \frac{k_s \epsilon_0}{e} \left(\frac{\partial n}{\partial E_F} \right)^{-1}$, [57] where n is the 2D carrier density. The form factor of the hard sphere which compares in the Alloy scattering rate in eq. 7f is substituted by the one of the hard disk in 2D. [58]

The validation of 2D *ElecTra*'s scheme is represented in **Figure A1**, where the DOS and band velocity for an isotropic parabolic band with effective mass equal to the electron rest mass, are compared with the known exact solutions in (a) and (b), respectively. The two methods (triangulation and nearest neighbour sampling) from **Section 3** are considered as well. With regards to the scattering treatment, an exact solution for the ADP and ODP scattering cases can also be obtained. *ElecTra*'s results are comparable with the analytical calculations in (c) and (d) for the TDF and the electrical conductivity, respectively.

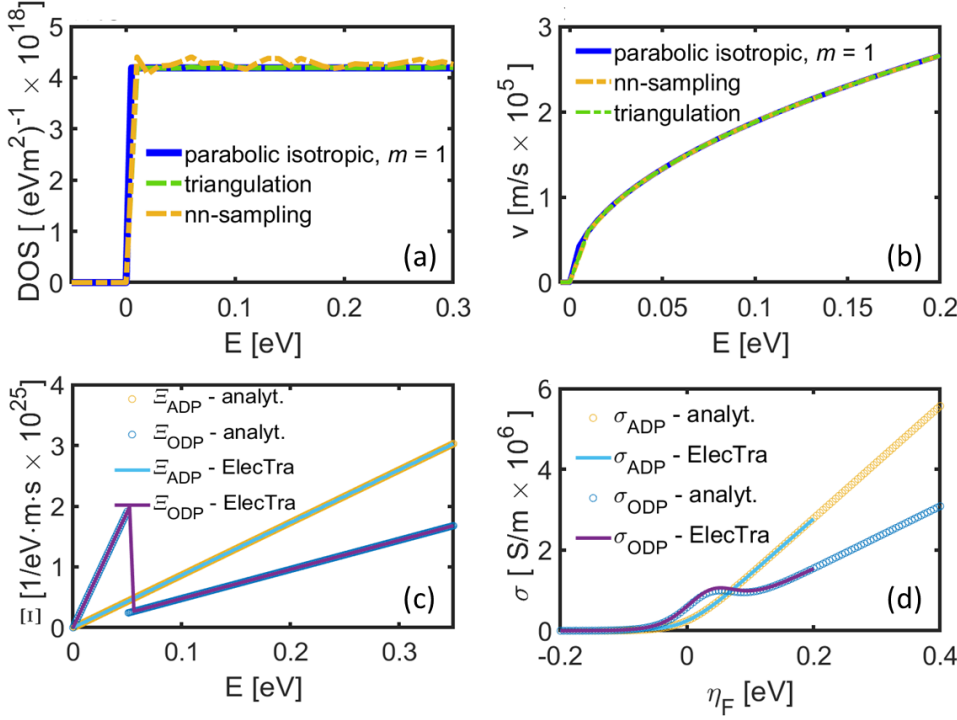


Figure A1: (a) Comparison of the DOS for a 2D parabolic band between the analytical value and the numerical one computed with *ElecTra*, by using the two BZ sampling techniques. (b) Same as in (a), for the band velocity comparison between the analytical solutions and numerical from *ElecTra*. (c) Comparison between the TDF computed with *ElecTra* with analytical known solutions for ADP and ODP scattering mechanisms. (d) Same as (c) for the electrical conductivity.

Appendix B – additional technicalities

In this appendix we provide some details of the code speed-up with parallelization and the available band interpolation. Additional information are provided in the Supporting Information and in the *ElecTra* manual.[59]

ElecTra is parallelized at the level of the carrier energy, and supports both local, multiple processors on the same node, and cluster, multiple processors on more nodes, parallelization. **Figure B1** shows the scaling performance, obtained on the CINECA Galielo100 cluster [60] on a single node, for bipolar calculations using TiNiSn considering ADP-IVS, ODP, POP and IIS mechanisms, four temperatures and 15 doping levels (for each polarity). The speed-up shown is compared to the execution time using 5 CPUs as the basis, for (a) the constant energy surface composition, and (b) the rates and TDF calculations. The times are evaluated with the ‘tic’-‘toc’ functions in MATLAB® and have around 5% of error. The times required to run the computations on 5 CPUs are for the formation of constant energy surfaces are around 40 s and 70 s for conduction and valence bands

respectively. For the scattering rates and transport coefficients calculations, they are 6.5 hr and 21.7 hr for the conduction and valence band, respectively. **Figure B1d** shows interpolation results for the DOS of the TiCoSb valence band. These interpolations take around 15 minutes and 45 minutes for interpolating an initial $51\times$ mesh to a $101\times$ and $151\times$ meshes, respectively, on a laptop, which is similar time compared to the interpolation performed using Wannier interpolations, which can also be used an alternative method.

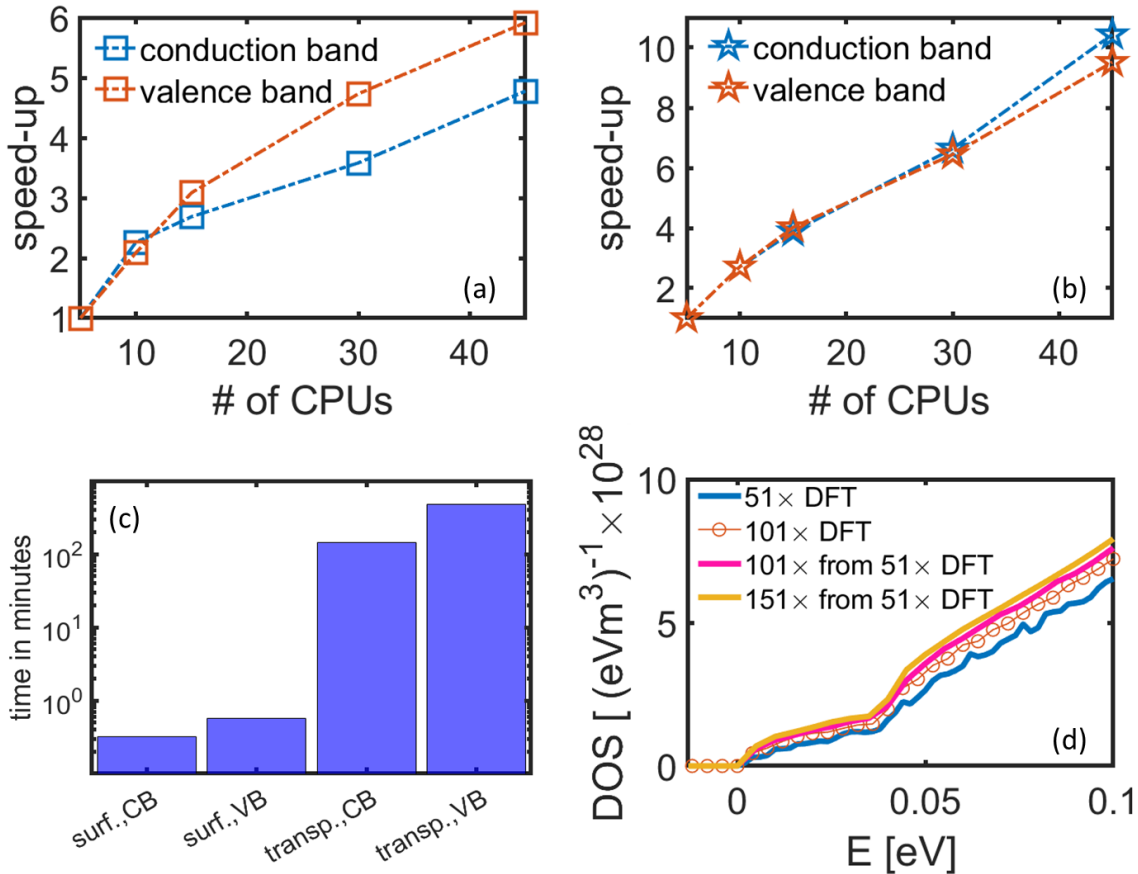


Figure B1: HPC speed-up in compared to a simulation of using 5 CPUs for: (a) the constant energy surfaces formation, and (b) the scattering times calculation. (c) Computation times for the case of 10 CPUs and the case detailed in the text as an example, for the computation of the constant energy surfaces, surf., and the scattering rates and transport coefficients, transp., for CB and VB, as indicated. (d) Numerical interpolation example for the TiCoSb DOS; solid lines are for a DFT mesh of $51\times 51\times 51$ points and its interpolation, and compared to the results when using a $101\times 101\times 101$ DFT mesh (red circles).

- References**
- 1 W. G. Zeier, A. Zevalkink, Z. M. Gibbs, G. Hautier, M. G. Kanatzidis, and G. J. Snyder, *Angew. Chem., Int. Ed.* 55, 6826 (2016).
 - 2 "D. Beretta, N. Neophytou, J. M. Hodges, M. G. Kanatzidis, D. Narducci, M. Martin-Gonzalez, M. Beekman, B. Balke, G. Cerretti, W. Tremel, A. Zevalkink, A. I. Hofmann, C. Müller, B. Dörling, M. Campoy-Quiles, and M. Caironi, *Mater. Sci. Eng. R* 138, 100501 (2019)."
 - 3 Y. Zheng, T. J. Slade, L. Hu, X. Y. Tan, Y. Luo, Z.-Z. Luo, J. Xu, Q. Yan, and M. G. Kanatzidis *Chem. Soc. Rev.*, 50, 9022 (2021).
 - 4 Q. Yan and M. G. Kanatzidis, *Nat. Mater.* (2021) , 10.1038/s41563-021-01109-w
 - 5 P. Graziosi, C. Kumarasinghe, N. Neophytou, *J. Appl. Phys.* 126, 155701 (2019)
 - 6 E. Witkoske, X. Wang, J. Maassen, and M. Lundstrom, *Mater. Today Phys.* 8, 43 (2019)
 - 7 N. Neophytou, *Theory and Simulation Methods for Electronic and Phononic Transport in Thermoelectric Materials* (Springer) 2020
 - 8 N. Neophytou, V. Vargiamidis, S. Foster, P. Graziosi, L. de Sousa Oliveira, D. Chakraborty, Z. Li, M. Thesberg, H. Kosina, N. Bennett, G. Pennelli, and D. Narducci, *Eur. Phys. J. B* 93, 213 (2020)
 - 9 P. Graziosi, C. Kumarasinghe, N. Neophytou, *ACS Appl. Energy Mater.* 3, 5913 (2020)
 - 10 C. Rudderham and J. Maassen, *J. Appl. Phys.* 127, 065105 (2020)
 - 11 C. Rudderham and J. Maassen, *Phys. Rev. B* 103, 165406 (2021)
 - 12 G. Madsen, D. Singh, *Comput. Phys. Comm.*, 175, 6771 (2006)
 - 13 G. Pizzi, D. Volja, B. Kozinsky, M. Fornari, N. Marzari, *Comput. Phys. Comm.*, 185, 422 (2014)
 - 14 T. Sohler, D. Campi, N. Marzari, M. Gibertini, *Phys. Rev. Materials* 2, 114010 (2018)
 - 15 G. Samsonidze and B. Kozinsky, *Adv. Energy Mater* 8, 1800246 (2018)
 - 16 S. Smidstrup et al., *Journal of Physics: Condensed Matter*, 32, 015901 (2019)

- 17 J. Park, Y. Xia, A. M. Ganose, A. Jain, and V. Ozoliņš, *Phys. Rev. Applied* 14, 024064 (2020)
- 18 A. M. Ganose, J. Park, A. Faghaninia, R. Woods-Robinson, K. A. Persson, and A. Jain, *Nat. Commun.* 12, 2222 (2021)
- 19 J.-J. Zhou, J. Park, I-Te Lu, I. Maliyov, X. Tong, and M. Bernardi, *Comput. Phys. Commun.* 264, 107970 (2021)
- 20 T. Deng, G. Wu, M. B. Sullivan, Z. M. Wong, K. Hippalgaonkar, J.-S. Wang, and S.-W. Yang, *npj Computational Materials*, 6, 46 (2020)
- 21 M. Lundstrom, *Fundamentals of Carrier Transport* (Cambridge University Press, 2000)
- 22 B. R. Nag, *Electron Transport in Compound Semiconductors* (Springer-Verlag Berlin Heidelberg, New York, 1980)
- 23 P. Graziosi and N. Neophytou, *J. Phys. Chem. C* 124, 18462 (2020)
- 24 P. Graziosi, Z. Li, and N. Neophytou, *Appl. Phys. Lett.* 120, 072102 (2022)
- 25 A. Kokalj, *J. Mol. Graphics Modelling*, 17, 176 (1999).
- 26 Code available from <http://www.xcrysden.org/>.
- 27 G. Lehmann and M. Taut, *Phys. Status Solidi B* 54, 469 (1972)
- 28 N. Neophytou, H. Karamitaheri and H. J. J. o. C. E. Kosina, *J. Comput. Electron.* 12, 611 (2013).
- 29 P. Giannozzi, S. Baroni, N. Bonini, M. Calandra, R. Car, C. Cavazzoni, D. Ceresoli, G. L. Chiarotti, M. Cococcioni, I. Dabo, A. Dal Corso, S. de Gironcoli, S. Fabris, G. Fratesi, R. Gebauer, U. Gerstmann, C. Gougoussis, A. Kokalj, M. Lazzeri, L. Martin-Samos, N. Marzari, F. Mauri, R. Mazzarello, S. Paolini, A. Pasquarello, L. Paulatto, C. Sbraccia, S. Scandolo, G. Sclauzero, A. P. Seitsonen, A. Smogunov, P. Umari and R. M. Wentzcovitch, *Journal of Physics: Condensed Matter* 21, 395502 (2009).
- 30 P. Giannozzi, O. Andreussi, T. Brumme, O. Bunau, M. Buongiorno Nardelli, M. Calandra, R. Car, C. Cavazzoni, D. Ceresoli, M. Cococcioni, N. Colonna, I. Carnimeo, A. Dal Corso, S. de Gironcoli, P. Delugas, R. A. DiStasio, A. Ferretti, A. Floris, G. Fratesi, G. Fugallo, R. Gebauer, U.

- Gerstmann, F. Giustino, T. Gorni, J. Jia, M. Kawamura, H. Y. Ko, A. Kokalj, E. Küçükbenli, M. Lazzeri, M. Marsili, N. Marzari, F. Mauri, N. L. Nguyen, H. V. Nguyen, A. Otero-de-la-Roza, L. Paulatto, S. Poncé, D. Rocca, R. Sabatini, B. Santra, M. Schlipf, A. P. Seitsonen, A. Smogunov, I. Timrov, T. Thonhauser, P. Umari, N. Vast, X. Wu and S. Baroni, *Journal of Physics: Condensed Matter* 29, 465901 (2017).
- 31 M.V. Fischetti, S.E. Laux, *J. Appl. Phys.* 80, 2234 (1996)
- 32 M. V. Fischetti, Z. Ren, P. M. Solomon, M. Yang and K. Rim, *J. Appl. Phys.* 94, 1079 (2003).
- 33 N. Neophytou and H. Kosina, *Phys. Rev. B* 83, 245305 (2011).
- 34 N. Neophytou and H. Kosina, *Phys. Rev. B* 84, 085313 (2011).
- 35 H. Ehrenreich, *J. Phys. Chem. Solids* 8, 130 (1959)
- 36 G. Klimeck, R. Lake, D. Blanks, C.L. Fernando, R.C. Bowen, T. Moise, and Y.C. Kao, *Phys. Status Solidi B* 204, 408 (1997).
- 37 J. Zhou, H. Zhu, T. H. Liu, Q. Song, R. He, J. Mao, Z. Liu, W. Ren, B. Liao, D. J. Singh, Z. F. Ren, and G. Chen, *Nat. Commun.* 9, 1721 (2018).
- 38 Q. Ren, C. Fu, Q. Qiu, S. Dai, Z. Liu, T. Masuda, S. Asai, M. Hagihala, S. Lee, S. Torri, T. Kamiyama, L. He, X. Tong, C. Felser, D. J. Singh, T. Zhu, J. Yang, and J. Ma, *Nat. Commun.* 11, 3142 (2020).
- 39 D. Archetti, N. Neophytou, *Molecules* 25, 5350 (2020)
- 40 <https://materialsproject.org/materials/mp-5967/#dielectric-props>
- 41 C. Jacoboni, C. Canali, G. Ottaviani, A. Alberigi Quaranta, *solid-State Electronics* 20, 77, (1977)
- 42 V. I. Fistul, M. I. Iglitsyn, and E. M. Omelyanovskii, *Sov. Phys. Solid State* 4, 784 (1962)
- 43 Landoldt-Bornstein, *Numerical Data and Functional Relationships in Science and Technology*, New Series Group III, Vol. 17a, Springer, Berlin, 1982
- 44 M. Sotoodeh, A. H. Khalid, and A. A. Rezazadeh, *J. Appl. Phys.* 87, 2890 (2000)
- 45 W Fawcett and E G S Paige, *J. Phys. C: Solid St. Phys.*, 4, 1801, 1971

- 46 Z. Li, P. Graziosi, and N. Neophytou, *Phys. Rev. B* 104, 195201 (2021).
- 47 A. R. Murphy, F. Murphy-Armando, S. Fahy, and I. Savić, *Phys. Rev. B* 98, 085201 (2018)
- 48 N. Neophytou and H. Kosina, *J. Comput. Electron.* 11, 29 (2012)
- 49 G. Ottaviani, L. Reggiani, C. Canali, F. Nava and A. Alberigi-Quaranta, *Phys. Rev. B* 12, 3318 (1975).
- 50 M. Markov, S. E. Rezaei, S. N. Sadeghi, K. Esfarjani, and M. Zebarjadi, *Phys. Rev. Materials* 3, 095401 (2019)
- 51 S E. Rezaei, M. Zebarjadi, and K. Esfarjani, *J. Solid State Chem.*, 302, 122414 (2021).
- 52 v-joe (<https://physics.stackexchange.com/users/217296/v-joe>), Screening of a coulomb-like potential, <https://physics.stackexchange.com/q/450055> (version: 2018-12-24); <https://blog.cupcakephysics.com/electromagnetism/math%20methods/2014/10/04/the-fourier-transform-of-the-coulomb-potential.html> ; BGreen (<https://math.stackexchange.com/users/220293/bgreen>), Fourier transform of the 2D Coulomb potential, <https://math.stackexchange.com/q/3627267> (version: 2020-04-14)
- 53 T. Sohler, M. Calandra, and F. Mauri, *Phys. Rev. B* 94, 085415 (2016)
- 54 T. Sohler, M. Gibertini, M. Calandra, F. Mauri, and N. Marzari, *Nano Lett.* 17, 3758 (2017)
- 55 J. Ma, D. Xu, R. Hu, X. Luo, *J. Appl. Phys.* 128, 035107 (2020)
- 56 M. Fischetti and S. Laux, *Phys. Rev. B* 48, 2244 (1993)
- 57 N. Neophytou, J. Guo, and M. Lundstrom, *IEEE Trans. Nanotech.*, 5, 385 (2006)
- 58 J. S. Pedersen, *Adv. Colloid Interface Sci.* **70**, 171 (1997)
- 59 DOI: 10.5281/zenodo.5074943
- 60 For the node performance, please see <https://www.hpc.cineca.it/hardware/galileo100>